Theoretical realization of two-dimensional half-metallicity and fully spin-polarized multiple nodal-line fermions in monolayer PrOBr

Lei Jin [1,2] Xiaoming Zhang,[1,2,*] Ying Liu,[2] Xuefang Dai,[2] and Guodong Liu[1,2,†]

[1]*State Key Laboratory of Reliability and Intelligence of Electrical Equipment, Hebei University of Technology, Tianjin 300130, China*
[2]*School of Materials Science and Engineering, Hebei University of Technology, Tianjin 300130, China*

Two-dimensional (2D) half metallicity and topological aspects of matter are the focus of current research because of the promising applications in nanoscale spintronics and quantum electronics. In this work, we report the perfect combination of half-metallic properties and electronic topological properties in single 2D phase, namely, the PrOBr monolayer. The material only possesses conducting electrons in the spin-up channel, while it shows a large insulating gap of 3.5 eV in the spin-down channel with the Curie temperature as high as 423 K. In the conducting spin channel, it exhibits multiple band crossings, which can surprisingly realize the coexistence of fully spin-polarized open/closed, and type-I/type-II/hybrid-type nodal lines. The coexistence of so many nodal line states has been neither identified in 2D materials nor identified in half metals before. The protection mechanism, the spin-orbit coupling impact, and the effective models for the nodal lines have been clarified. Our results suggest that the PrOBr monolayer is a good electronic material with (i) 2D half metallicity; (ii) multiple nodal lines of 100% spin polarization.

I. INTRODUCTION

Since the discovery of graphene [1], it has seen great research enthusiasm in two-dimensional (2D) materials [2–4]. The unique morphology endows 2D materials' diverse physical properties with the bulk counterparts and broad applications in nanoscale devices [5–8]. Unlike the nonmagnetic (NM) graphene, many 2D materials were proposed to show intrinsic ferromagnetism (FM) [9–13]. The low dimensionality in 2D FM allows free axes for device modulation as well as quantization of electronic states, which has triggered tremendous potential in the applications of spintronics and nonvolatile memories [14–17]. For these applications, a novel 2D FM category, namely, 2D half metal is highly desired due to it theoretically carries the 100% spin polarization [18–21]. Although many 2D half metals have been identified so far [19–31], most of them have relatively low Curie temperature (T_C) and small spin gap, which cannot realize high enough spin polarization for device operating at room temperature. As such, great effort has been made to explore 2D half metals with high (T_C) and large spin gap.

Topological states of matter have received growing interest due to their extraordinary electronic, transport, and electrochemical properties originating from the nontrivial band topology [32–45]. Liu *et al.* reported using all-carbon-based porous topological semimetal for lithium battery anode material [39]. Li *et al.* proposed that the topological nodal line is a good candidate for the hydrogen evolution reaction, because its drumhead-like nontrivial surface states provide a

robust platform to activate chemical reactions [40]. Among various topological aspects, nodal line state is currently under hot investigation owing to its unique continuous configuration of band crossing which brings in rich possibilities of topological structures [38,46–54]. For one aspect, nodal line state can show either open loops penetrating the entire Brillouin zone (BZ) or the closed ones not traversing the BZ. Their comparison is shown in Fig. 1(a). As demonstrated by Li *et al.* [55], the two forms of nodal lines are characterized by diverse topological Z^3 index. Quite recently, it has been also demonstrated in a 2D system [56] that open nodal lines can inherently carry longer edge states than the closed ones, as illustrated in Fig. 1(a). For another aspect, nodal line state can take different forms when taking into account the slope of crossing bands. As shown in Fig. 1(b), three categories, namely, type-I, type-II, and hybrid nodal lines can be typically termed [55,57]. Among them, type-I (or type-II) nodal lines purely show type-I (or type-II) band crossings [55,58–61], whereas hybrid nodal lines show both type-I and type-II band crossings [31,57,62,63]. The three categories of nodal lines show diverse transport, optical, and magnetic properties [55,57]. Therefore one may naturally wonder: Is it possible to realize all categories (open and closed; type-I, type-II, and hybrid) of nodal lines in one single material? Previously, the coexistence of multiple nodal lines was identified in few NM 3D materials including $FeSi_2$ and TiS [64,65]. However, such an occasion has not been realized in 2D limit or in half metals.

In the current work, on the basis of first principles, we propose a PrOBr monolayer as the first example of a 2D nodal line half metal with simultaneously realizing multiple nodal line categories in the low-energy band structure. We show that a PrOBr monolayer shows an excellent half-metallic state with
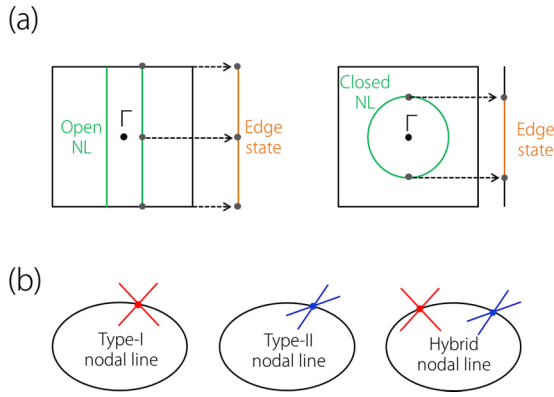
---

*zhangxiaoming87@hebut.edu.cn
†gdliu1978@126.com

FIG. 1. (a) Schematic diagram for an open/closed 2D nodal line (NL) and traversing/partial edge state. (b) Illustration of type-I, type-II, and hybrid nodal lines.

a high Curie temperature (423 K) and a large insulating gap (3.5 eV). In the conducting spin channel, a PrOBr monolayer features a total of five nodal lines near the Fermi level, which are fully spin-polarized. Remarkably, these nodal lines belong to different categories including closed/open nodal lines and type-I/hybrid nodal lines. The coexistence of so many categories of nodal line states has been never identified in 2D half metals before. We demonstrate that the nodal lines are protected by horizon mirror symmetry and are robust against spin-orbit coupling (SOC). In addition, effective models are constructed to capture the nature of nodal lines. This work reveals a good material platform to explore 2D half metallicity and various nodal-line fermions with fully spin polarization, which also hosts great potential for nanoscale spintronics and topological quantum applications.

II. COMPUTATIONAL METHODS

In this work, the first-principles calculations are performed by the Vienna *ab initio* Simulation Package (VASP) [66] using the projector augmented wave (PAW) method in the framework of density-functional theory (DFT) [67]. For the exchange-correlation potential, we use the generalized gradient approximation (GGA) of the Perdew-Burke-Ernzerhof functional [68]. For the crystal structure of the PrOBr monolayer, we build a vacuum space of 15 Å to avoid potential interactions between layers. During the calculations, the long-range van der Waals interactions are taken into account by using the DFT-D2 method [69]. The cutoff energy is set as 500 eV. A Γ-centered k mesh of $13 \times 13 \times 1$ is used for the BZ sampling. To investigate the dynamical stability of the PrOBr monolayer, we calculated the phonon spectra by using a 3×3 supercell. The force constants were calculated by VASP; the preprocess and postprocess were performed in the PHONOPY package [70] using density functional perturbation theory. The force and energy convergence criteria are applied as 0.001 eV/Å and 10^{-5} eV, respectively. The topological features of edge states were calculated based on the maximally localized Wannier functions [71] extracted from the plane-wave base of VASP. The posprocess used the WANNIERTOOLS package [72].
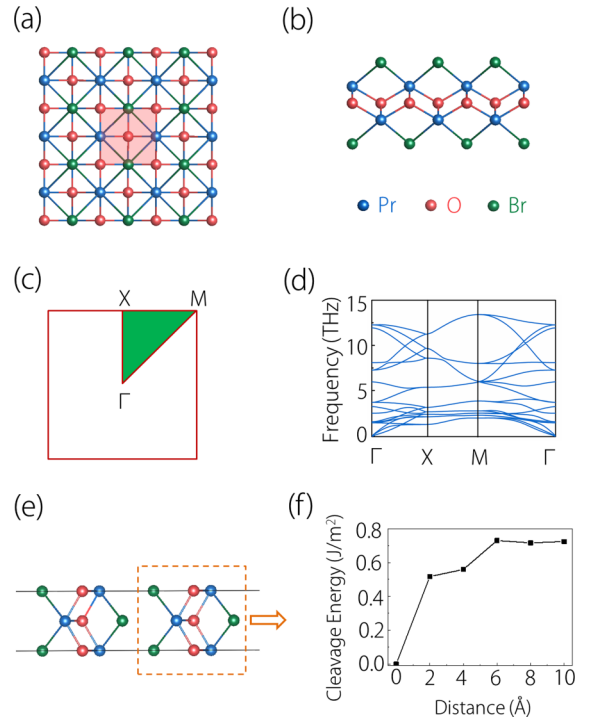

FIG. 2. (a) Top and (b) side views of the crystal structure for the PrOBr monolayer. The shadowed region in (a) shows its primitive cell. (c) The 2D BZ of the PrOBr monolayer. (d) The phonon spectrum of the PrOBr monolayer. (e) The two-layer (2L) slab is shown in the map. (f) Cleavage energy of PrOBr as a function of the separation distance between 1L and the remainder of the 2L slab. The distance changes from 0 to 10 Å, and the distance zero means the equilibrium distance of the bulk structure.

III. RESULTS AND DISCUSSIONS

A. Crystal structure, phase stability, and magnetic properties

The PrOBr monolayer has a 2D tetragonal lattice belonging to the space group P4/nmm. The lattice structure is shown in Figs. 2(a) and 2(b). In the top view [see Fig. 2(a)], the shadowed region shows the primitive cell of the PrOBr monolayer. One primitive cell contains two Pr atoms, two O atoms, and two Br atoms, respectively. Figure 2(b) shows the side view of the PrOBr lattice, which contains a quintuple layer of atoms stacked in the sequence of Br-Pr-O-Pr-Br. The lattice constant for PrOBr monolayer is optimized as $a = b = 4.100$ Å. The Pr-Br and Pr-O bond lengths are 3.364 and 2.375 Å, respectively. The structure of PrOBr monolayer was first reported by the Materials Cloud [73], which suggests that its monolayer form can be easily exfoliated from its 3D experimental crystal structure. We also calculate the cleavage energy to explore the possibility of fabricating the PrOBr monolayer from its layered bulk structure. As shown in Fig. 2(e), the two-layer slab method is used to simulate the exfoliation process. Figure 2(f) shows the cleavage energy increases by increasing the separation distance and it finally converges to about 0.72 J/m^2 at 6 Å. Compared with the cleavage energy of other 2D materials, such as graphene (0.37 J/m^2) [74], MoS_2 (0.55 J/m^2) [75], CP_3 (0.57 J/m^2) [76], GeP_3 (1.14 J/m^2) [77], InP_3 (1.32 J/m^2) [78], Ga_2N (1.09 J/m^2) [79], and
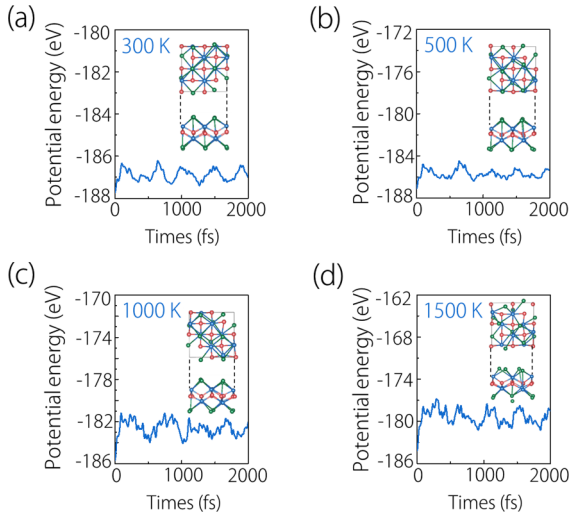
FIG. 3. Total potential energy fluctuations of the PrOBr monolayer during AIMD simulations at (a) 300 K, (b) 500 K, (c) 1000 K, and (d) 1500 K; the insets show the final state of the structure after AIMD simulations.
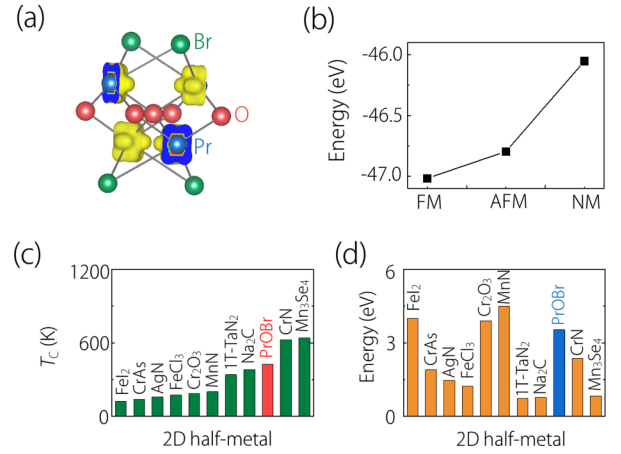

FIG. 4. (a) The spin density of the PrOBr monolayer. (b) Comparison of the energy among different magnetic states. (c) The Curie temperature of the PrOBr monolayer compared with the values of the previously reported 2D half metal. (d) Comparison of monolayer PrOBr with typical 2D half metal for the width of insulating gap. Some data in (c) and (d) were obtained from the literature [19,20,23,25–31].

Ca$_2$N (1.08 J/m^2) [79], the PrOBr monolayer is feasible to be exfoliated experimentally from the bulk structure.

To confirm the dynamic stability of PrOBr, the phonon spectra calculation was performed in a 3×3 supercell. As shown in Fig. 2(d), the phonon spectra exhibit no imaginary mode throughout all high-symmetry k paths in the 2D BZ. Thus the given structure of the PrOBr monolayer has an excellent dynamical stability. Besides, we also investigate the thermal stability of the PrOBr monolayer by using the *ab initio* molecular dynamic (AIMD) calculation. In the AIMD simulation, the 2×2 supercell of the PrOBr monolayer is applied. The temperature was set as 300, 500, 1000, and 1500 K, respectively, with 1000 steps (2 fs for each step) of simulation. As shown in Figs. 3(a)–3(d), we can observe that the lattice of the PrOBr monolayer is almost retained at 300, 500, 1000, and 1500 K. These results show that the PrOBr monolayer possesses good thermal stability as well.

The Materials Cloud suggests that the PrOBr monolayer has a FM ground state with the magnetization along the out-of-plane [001] direction [73]. In this work, we have also checked the magnetic ground state of the PrOBr monolayer. Figure 4(a) shows the spin charge density of the PrOBr monolayer. We can find that the magnetism is mainly contributed by the Pr element. Further, as shown in Fig. 4(b), we compare the total energy of the PrOBr monolayer without SOC and under the NM, FM, and antiferromagnetic (AFM) states. The results show that the FM state is 0.22 eV lower than the AFM state and 0.96 eV lower than the NM state for one unit cell, confirming the FM ground state in the PrOBr monolayer; we also determine the ground magnetic configuration in the case of SOC. We compare the total energies among FM and AFM and consider three magnetization directions with the highest potential, including [0 0 1], [1 0 0], and [1 1 0], in each magnetic state. The results are summarized in Table I. It can be seen that the energy is lowest in [0 0 1] of the FM state. Therefore, in the case of SOC, the magnetic ground state is still FM, and the easy magnetic

axis is [0 0 1]. In the magnetic ground state, the magnetic anisotropy energies (MAE = $E_{[100]or[110]}$-$E_{[001]}$) of the other two directions [1 0 0] and [1 1 0] are 55 and 50 meV/cell, respectively. We also compare the magnitudes of MAE (55 meV/cell) in PrOBr with other 2D FM materials, including CrAs (1.2 meV/cell) [25], YN$_2$ (0.088 meV/cell) [80], CsS (1.28 meV/cell) [81], CrI$_3$ (1.37 meV/cell) [82], Fe$_3$GeTe$_2$ (2.76 meV/cell) [83], Fe$_2$Ge (1.21 meV/cell) [84], Fe$_2$Sn (1.78 meV/cell) [84], InC (0.4 meV/cell) [59], and MnN (0.4 meV/cell) [29]. The results show that the magnitude of MAE in PrOBr is very large and much larger than the above typical FM materials; thus it barely change the spin orientations by external magnetic field. Under the ground state, the PrOBr monolayer has an integer magnetic moment of 4.0 μB, which almost originates from the Pr element. In addition, we also estimate the value of T_C for the FM state under the Monte Carlo simulation. The simulation is on the basis of a classical Heisenberg-like spin model [85],

$$H = -\mathcal{J} \sum_{\langle i,j \rangle} S^i \cdot S^j - \mathcal{K} \sum_i (S_z^i)^2; \qquad (1)$$

in the model, the parameter S is the net magnetic moment at the Pr site, i and j label the Pr sites, and $\langle i, j \rangle$ denotes the nearest-neighboring sites. $\mathcal{J}$ represents the exchange parameter. By mapping the DFT energies to the Heisenberg model, $\mathcal{J}$

TABLE I. The energy ΔE per unit cell (in meV, relative to that of the FM with [0 0 1] ground state). The values are calculated by the GGA+SOC method.

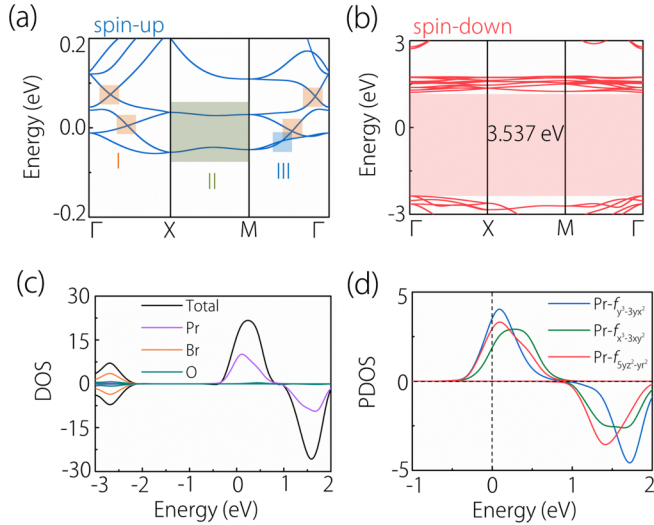|	FM	AFM
[0 0 1]	0	49
[1 0 0]	55	55
[1 1 0]	50	55

FIG. 5. The electronic band structures of the PrOBr compound in the absence of SOC. (a) Spin-up band structure showing a metallic character with several nodal lines near the Fermi level. (b) Spin-down band structure exhibiting an insulating character with a big band gap of 3.537 eV. (c) The total DOS and (d) The PDOS of the PrOBr monolayer.

FIG. 6. (a) The spin-up band structures of the PrOBr compound along the M-Γ-X path. Band crossings A and C are in nodal loop L_1. Band crossings B and D are in nodal loop L_2. (b) The 3D plot of band dispersion near nodal loops L_1 and L_2. (c) and (d) The shape of nodal loops L_1 and L_2 in the PrOBr compound. L_1 and L_2 are both type-I nodal loops.

can be calculated as $\mathcal{J} = \Delta E/(8S^2)$, where ΔE is the energy difference between the FM and the AFM order under the easy magnetic axis, leading to the exchange coupling parameter of 1.23×10^{-22} J; the $\mathcal{K}$ parameter represents the magnetic anisotropy strength. $\mathcal{K}$ could be evaluated by calculating the MAE $E_{(\text{MAE})} = E_{[\text{in-plane}]} - E_{[\text{out-of-plane}]}$ and expressed as $\mathcal{K} = E_{(\text{MAE})}/S^2$. The magnetic anisotropy strength is $\mathcal{K} = 1.1 \times 10^{-21}$ J. During the simulation, a 100×100 supercell of the PrOBr monolayer is applied. The estimated T_C for the PrOBr monolayer is about 423 K, which is higher than typical 2D half metals as shown in Fig. 4(c).

B. Electronic band structure

Here we investigate the electronic band structure of the PrOBr monolayer. The band structure for the spin-up and spin-down channels are shown in Figs. 5(a) and 5(b), respectively. We clearly observe a half-metallic band structure for the PrOBr monolayer, where the spin-up band is metallic while the spin-down one is insulating. Thus the conducting electrons in the PrOBr monolayer have 100% spin polarization. By examining the total density of states (DOS) and the projected density of states (PDOS), we find that the low-energy states in the PrOBr monolayer are mainly contributed by the f orbitals of Pr atoms, as indicated in Figs. 5(c) and 5(d). Besides T_C, the size of insulating gap is another crucial judgment for half metals. As indicated in Fig. 5(b), the insulating band gap in the PrOBr is as large as 3.537 eV. In Fig. 4(d), we compare the insulating gap size of typical 2D half metals. We can observe that the value for PrOBr monolayer is among the largest insulating gaps. Combing with high T_C and large insulating gap, the PrOBr monolayer can serve as an excellent 2D half-metal candidate.

Here we pay attention to the band structure in the conducting spin channel. As shown in Fig. 5(a), we find that the bands
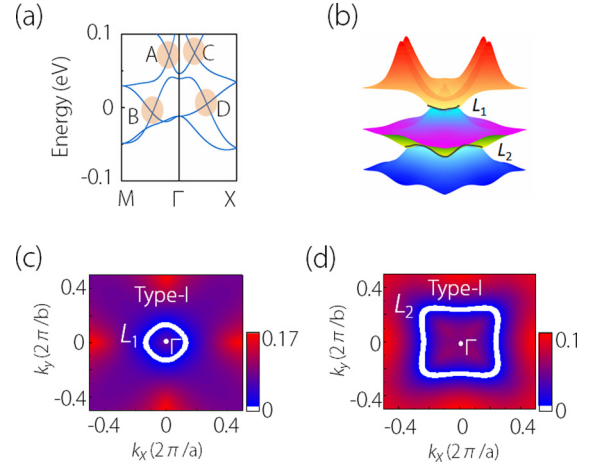
near the Fermi level (within ± 0.1 eV) show multiple band crossings. For sample, we divide the band crossings into three groups for further discussion, which are labeled with I, II, and III in Fig. 5(a). We first discuss group I, which contains four band crossings. In Fig. 6(a), we display the enlarged band structure for group I and label the four band crossings as A, B, C, and D, respectively. Our further study finds these band crossings are not isolated but belong to two nodal lines around the Γ point in the 2D BZ. The 3D plotting of the crossing bands is shown in Fig. 6(b), where the two nodal lines are labeled as L_1 and L_2, respectively. The crossings A and C are at a higher energy level and locate on nodal line L_1, whereas crossings B and D locate on nodal line L_2. The profiles for nodal lines L_1 and L_2 are indicated in Figs. 6(c) and 6(d), respectively.

By observing the profiles of nodal lines L_1 and L_2, we find that both belong to closed nodal lines. Such closed nodal lines have also been reported in several 2D magnetic materials including the CrN monolayer [31], the MnN monolayer [29], and the K_2N monolayer [51]. As illustrated in Fig. 1(a), 2D closed nodal lines show partial edge states which do not traverse the BZ boundary. To show this point, we calculate the edge states for nodal lines L_1 and L_2 corresponding to different edge projections. The edge projections and corresponding edge states are shown in Figs. 7(a)–7(d), respectively. The edge states for nodal lines L_1 and L_2 can be clearly identified. In addition, by examining the band slopes around nodal lines L_1 and L_2 [see Figs. 6(a) and 6(b)], we find both L_1 and L_2 are solely composed of type-I crossings, suggesting they belong to type-I nodal lines.

For group II, we show the enlarged band structure in Fig. 8(a). This group shows two doubly degenerate bands throughout the $X - M$ path in the 2D BZ. Such doubly degenerate bands in fact can be seen as nodal lines traversing the whole BZ, as shown in Fig. 8(b). Here we denote the two nodal lines as L_3 and L_4. On the nodal lines, every point takes
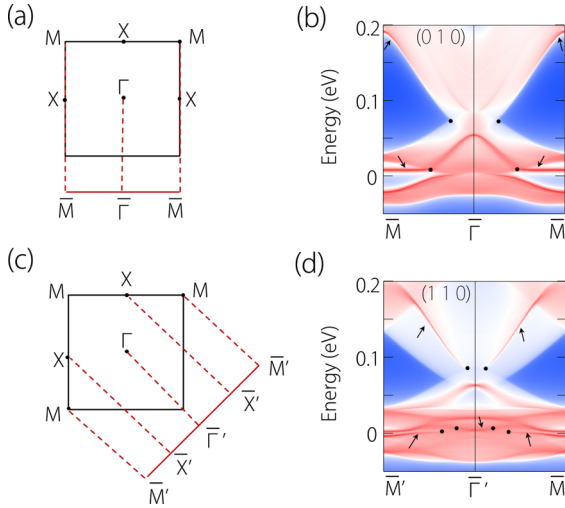
FIG. 7. (a) and (b) The projection of 2D BZ onto the (010) edge and the surface band structure of PrOBr. (c) and (d) Its projection onto the (110) edge and corresponding surface band structure of PrOBr. The surface bands for the nodal loop L_1 and L_2 are pointed by the black arrows. The black points indicate the position of the projected nodal points.

the form of a linear band crossing. This phenomenon can be traced by showing band structures along k paths perpendicular to $X - M$. We show four new k paths ($a - a'$, $b - b'$, $c - c'$, and $d - d'$) and corresponding band structures in Figs. 8(b) and 8(c), respectively. We indeed observe two band crossings on each k path, which correspond to the two nodal lines at the $X - M$ path. Considering the slope of the bands, the nodal lines L_3 and L_4 both belong to type-I. However, these nodal lines are open nodal lines, which are different than the closed L_1 and L_2. Besides carrying a nontrivial topological index [55], open nodal lines are proposed to show extreme long
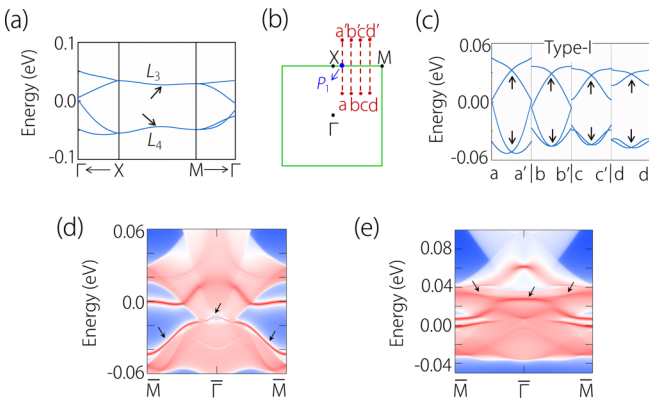

FIG. 8. (a) The electronic band structure of the PrOBr monolayer around L_3 and L_4 nodal lines. (b) The k-paths a-a', b-b', c-c', and d-d' are shown in the figure. The green lines represent L_3 and L_4, which overlap. (c) The enlarged electronic band structure along the a-a', b-b', c-c', and d-d' paths. All band crossings are type-I. (d) The projected spectrum on the (010) edge. The edge states indicated by the black arrow correspond to L_4. (e) The projected spectrum on the (110) edge. The edge states indicated by the black arrow correspond to L_3.
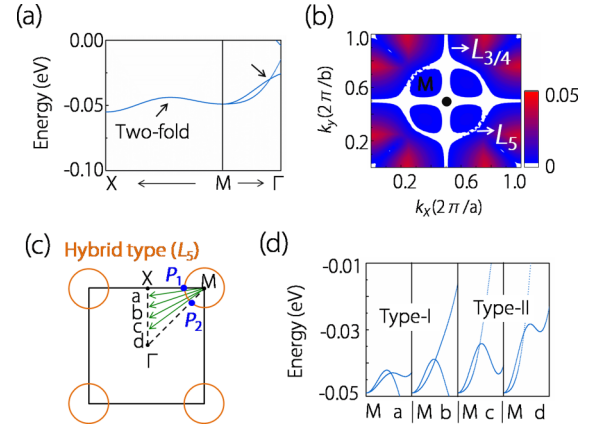

FIG. 9. (a) The electronic band structure of the PrOBr monolayer around the L_5 nodal loop. (b) The shape of nodal lines $L_{3/4}$ and L_5 in the PrOBr compound. $L_{3/4}$ is type-I open nodal line, as shown in Figure 8. L_5 is a hybrid-type nodal loop. (c) The selected k paths (M-a, M-b, M-c, M-d) through the nodal loop. The points a, b, c, and d are equally spaced between X and Γ. (d) The enlarged electronic band structure along the M-a, M-b, M-c, and M-d paths. There are both type-I and type-II band crossings.

edge states that can transverse the entire BZ boundary [56]. We calculate the edge states for the edge projections shown in Figs. 7(a) and 7(c), and the specific edge states are displayed in Figs. 8(d) and 8(e). We indeed observe long edge states traversing the entire edge boundary.

At last, we discuss the band crossing point in group "III". The enlarged band structure is shown in Fig. 9(a). Group III shows a type-II band crossing in the $M - \Gamma$ path. Our further calculation shows the band crossing is not isolated but actually belongs to a nodal line. Here we denote the nodal line as L_5. The profile of L_5 is shown in Fig. 9(b). Nodal line L_5 is a closed loop which centers the M point in the 2D BZ. To be noted, in Fig. 9(b) we can also observe the profile for the open nodal lines L_3 and L_4, which cross through L_5. Very interestingly, unlike $L_1 - L_4$, we find L_5 is in fact a hybrid nodal line. As shown by the band structures along the nodal lines in Fig. 9(d), we can observe that some parts of the nodal line show type-I band crossings while others show type-II crossings. Such hybrid nodal loops have also been proposed in several NM examples such as Ca_2As [57], Li_2BaSi [62], CrP_2O_7 [63], and the FM CrN monolayer [31]. However, except for CrN [31], the situation in the PrOBr monolayer is different with these examples, that the hybrid nodal line proposed here is completely spin-polarized because it originates from the bands in a single spin channel.

The above discussions show that the PrOBr monolayer totally contains five nodal lines (L_1-L_5) near the Fermi energy. These nodal lines share the same protection mechanism of the horizon M_z mirror symmetry. This requires that crossing bands have opposite M_z eigenvalues, which have been confirmed by our calculations, even though these nodal lines show different features. Among them, L_1, L_2, and L_5 are closed nodal lines, while L_3 and L_4 are open lines. Open nodal lines are found to show longer edge states than those of closed lines. Moreover, considering the band slope, L_1, L_2, L_3, and L_4 are traditional type-I nodal lines, whereas L_5 is a hybrid nodal
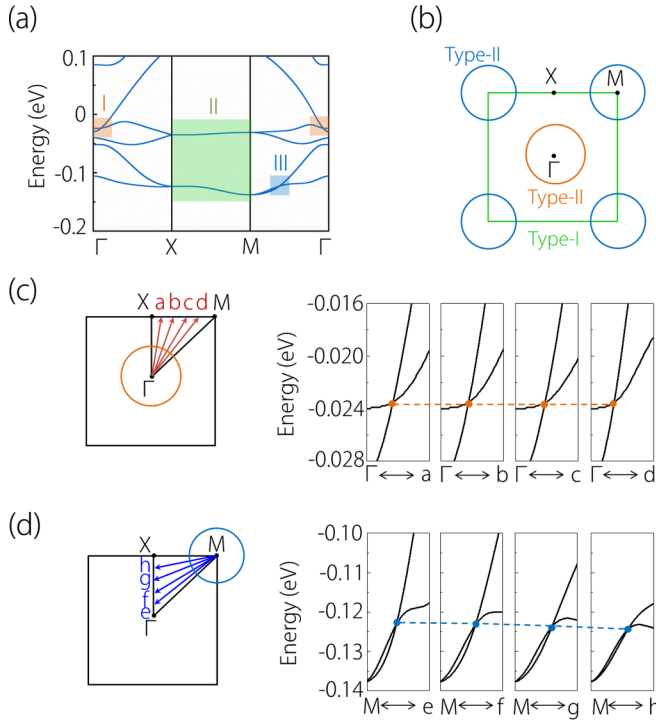
FIG. 10. (a) The band structure of PrOBr with SOC under [001] magnetization. Due to the protection of M_z symmetry, there are multiple-type nodal lines. (b) Along the boundary of the entire BZ, there are two open type-I nodal lines. In the center and four corners of the BZ, there are also type-II nodal loops around the Γ and M points. (c) The points a, b, c, and d are equally spaced between X and M. The enlarged electronic band structure is along the Γ-a, Γ-b, Γ-c, and Γ-d paths. All band crossings are type-II; thus the nodal loop around Γ is also type-II. Similar to (c), (d) shows that the points h, g, f, and e are equally spaced between X and Γ. The enlarged electronic band structure is along the M-e, M-f, M-g, and M-h paths. All band crossings are type-II; thus the nodal loop around M is also type-II. The dashed lines in (c) and (d) serve as a guide for the eye.

line. The hybrid nodal line can show diverse transport and magnetic response with type-I nodal line [57]. To be noted, the coexistence of so many different nodal lines has been rarely identified in 2D half metals before.

The above discussions are based on the electronic band structure without considering SOC. Remarkably, we find most band crossings persist when SOC is included, as shown in Fig. 10(a). The band crossings can also form nodal line structures. This can also be understood from the symmetry view. Noticing the magnetization is along the out-of-plane [001] direction, the M_z symmetry would retain under SOC. Our further calculation shows the crossing bands for all nodal lines show opposite M_z eigenvalues ($+i$ and $-i$, respectively), which verifies the protection of nodal lines. However, we find some nodal lines shift band slopes under SOC. For example, nodal line L_1 transforms from a type-I nodal line into a type-II nodal line, as shown by the specific band structure in Fig. 10(c). A similar phenomenon also happens in nodal line L_5, which has transformed from a hybrid nodal line into a type-II nodal line, as shown in in Fig. 10(d). As the result, the PrOBr monolayer can show type-II nodal lines under SOC.

To be noted, the spin-polarized type-II nodal line was only proposed in 3D half metals [61] but has not been identified in 2D half metals before.

C. Effective model

To further understand the appearance of nodal lines in the PrOBr monolayer, we construct effective $k \cdot p$ models for the band structure near the Fermi level. We first consider the case without SOC. Noticing that L_1 and L_2 have similar features, we here take L_1 as an example. The little group at the Γ point belongs to D_{4h}, which is generated by the following symmetries: The fourfold rotation C_{4z}, the twofold rotation C_{2z}, the twofold rotation C_{2y}, and inversion symmetry P. From the DFT result, it is identified that the three low-energy states at the Γ point belong to the following irreducible representations: E_u and B_{2u}. For E_u the two basis functions can be chosen as $\{x, y\}$. Such that the basis at this point can be generated by them, specifically, $B_{2u} \bigoplus E_u$, the three states as basis and denote them by $\{(x^2\text{-}y^2)z, x, y\}$. Under this basis, the symmetry operators have their corresponding matrix representations, denoted as $\mathcal{O}(R)$. Here, $\mathcal{O}$ runs over all of the symmetries, R is the actions on momentum space.

$$\mathcal{O}(C_{4z}) = \begin{bmatrix} -1 & 0 & 0 \\ 0 & 0 & 1 \\ 0 & -1 & 0 \end{bmatrix}, \quad \mathcal{O}(C_{2z}) = \begin{bmatrix} 1 & 0 & 0 \\ 0 & -1 & 0 \\ 0 & 0 & -1 \end{bmatrix},$$

$$\mathcal{O}(C_{2y}) = \begin{bmatrix} -1 & 0 & 0 \\ 0 & -1 & 0 \\ 0 & 0 & 1 \end{bmatrix}, \tag{2}$$

and $\mathcal{O}(P) = -I_{3\times3}$. To be noted, when SOC is absent, we only consider a single channel, say the spin-up channel, which respects the time-reversal symmetry, and $\mathcal{O}(\mathcal{T}) = \mathcal{K}$, $\mathcal{K}$ is the complex conjugation. The symmetry constraints on the Bloch Hamiltonian $\mathcal{H}(\boldsymbol{k})$ are

$$\mathcal{O}\mathcal{H}(R^{-1}k)\mathcal{O}^{-1} = \mathcal{H}(k). \tag{3}$$

Thus the overall effective Hamiltonian can be expressed as

$$\mathcal{H}(k) = \begin{bmatrix} M + B_0(k_x^2 + k_y^2) & 0 & 0 \\ 0 & B_1(k_x^2 - k_y^2) & A k_x k_y \\ 0 & A k_x k_y & -B_1(k_x^2 - k_y^2) \end{bmatrix}. \tag{4}$$

Here, M, B_0, B_1 and A are real coefficients related to specific materials. Away from the Γ point, the band with B_{2u} will cross with one of the bands with E_u. The effective model can be obtained from Eq. (4). After straightforward calculation, by expanding up to the quadratic order, the effective model can be written in the form as

$$\mathcal{H}_{L_1}(k) = (C + B_0' k_x^2 + B_1' k_y^2)I_{2\times2} + (-C + B_0' k_y^2 + B_1' k_x^2)\sigma_z. \tag{5}$$

Here $C = M/2$, $B'_{0/1} = (B_0 \pm B_1)/2$. The Hamiltonian characterizes a type-I nodal line, which is just the case for L_1 in the PrOBr monolayer. When $|B'_0| > (<) |B'_1|$, it will be tilted along k_x (k_y) directions. In the presence of SOC, C_{2y} and time-reversal symmetries are broken; D_{4h} is transformed into C_{4h}. Finally, L_1 could be transformed into a type-II nodal loop.

Unlike L_1 and L_2, L_3 and L_4 are open nodal lines. For example, L_3 is enforced by the combination of a screw rotation and time-reversal symmetry. This system belongs to Layer group 64, which hosts the screw rotation $C_{2y}:(x, y, z) \rightarrow (-x, y + 1/2, -z)$. The combination operation $\mathcal{T}C_{2y}$ only reverses the k_y, such that path $X - M$ is invariant under it. Along this path, one has

$$(\mathcal{T}C_{2y})^2 = e^{-ik_y} = -1. \tag{6}$$

It implies that there is a Kramer-like degenerate on path $X - M$. In order to identify the dispersion of L_3, we take a generic point on this path denoted as P_1 with respect to C_{2x}, M_y, and $P\mathcal{T}$ symmetries. There is a 2D irreducible representation Γ_1; regarding it as the basis, these operations can be given by

$$\mathcal{O}(C_{2x}) = i\sigma_y, \mathcal{O}(M_y) = \sigma_z, \mathcal{O}(P\mathcal{T}) = \mathcal{K}. \tag{7}$$

According to Eq. (3), one could derive the effective model for the generic point P_1,

$$\mathcal{H}(q) = C + c_1 q_x \sigma_0 + c_2 q_y \sigma_x. \tag{8}$$

Here q is measured from the crossing point along $a - a'$. This model indicates that the nodal line consists of type-I nodal point, because the tilted term $q_y \sigma_0$ is disallowed by M_y and/or C_{2x}.

Finally, we turn to the case of L_5, which is a hybrid nodal line without SOC. The hybrid nodal line can be generally described by the following Hamiltonian:

$$\mathcal{H}_{L_5}(k) = (C + c_1 k_x^2 + c_2 k_y^2)\sigma_0 + (C_0 + c_3 k_x^2 + c_4 k_y^2)\sigma_z$$
$$+ c_5 k_x k_y \sigma_x. \tag{9}$$

As seen in Fig. 9, the nodal point on L_5 along $X - M$ takes the type-I form, while it is a type-II nodal point along Γ-M. It can be demonstrated by the effective model around the crossing points. For example, the nodal point like P_1 along $X - M$ can be described by Eq. (8), which is a type-I nodal point. On the contrary, crossing point P_2 along Γ-M is described by the effective model

$$\mathcal{H}(q) = [M_0 + c_1(q_x + q_y)]\sigma_0 + [M_1 + c_2(q_x + q_y)]\sigma_z. \tag{10}$$

When $c_1 > c_2$, it shows a type-II nodal point as shown in Fig. 9. As a consequence, the nodal loop L_5 around M is a hybrid loop.

When SOC is included, it still has $(\mathcal{T}C_{2y})^2 = -1$, and the nodal lines L_3 and L_4 along $X - M$ are robust against the

magnetization along [0 0 1]. It is just that the energy of the L_3 and L_4 node lines decline overall. In addition, although the mirror symmetry (M_y) and the rotation symmetry (C_{2x}) are broken, this material still hosts their combination (C_{2z}), such that the perturbation term

$$\mathcal{H}_\delta(q) = c_3 q_y \sigma_0 + c_5(q_x - \Delta)\sigma_x \tag{11}$$

is allowed. When $|c_3| > (<) |c_2|$, it could be a type-II (type-I) point along $X - M$. In our work, the original nodal loop L_5 is transformed into a type-II nodal loop.

IV. SUMMARY

In summary, the phase stability, magnetic feature, and topological electronic structure of the PrOBr monolayer have been systematically investigated. It has been verified that the material has good dynamical stability and naturally takes a FM ground state. Under this ground state, the material exhibits a half-metal band structure. Especially from both the Curie temperature and the insulating gap views, the PrOBr monolayer is better than most 2D half metals identified before, making it a potential of applications in nanoscale spintronics. More remarkably, in the conducting channel the material can realize several different categories of nodal lines near the Fermi level, including closed nodal lines, open nodal lines, type-I nodal lines, and hybrid nodal lines. From the symmetry view, we illustrate that nodal lines are robust against SOC. In addition, effective models have been constructed to clarify the nature of the nodal lines. Our work suggests that the PrOBr monolayer is a good electronic material for combining high-temperature 2D half metallicity and multiple categories of nodal-line fermions.

[1] K. S. Novoselov, A. K. Geim, S. V. Morozov, D. Jiang, Y. Zhang, S. V. Dubonos, I. V. Grigorieva, and A. A. Firsov, Science **306**, 666 (2004).

[2] M.-B. Rubn, G.-N. Cristina, G.-H. Julio, and Z. Flix, Nanoscale **3**, 20 (2011).

[3] K. S. Novoselov, A. Mishchenko, A. Carvalho, and A. H. Castro Neto, Science **353**, aac9439 (2016).

[4] S. Das, J. A. Robinson, M. Dubey, H. Terrones, and M. Terrones, Annu. Rev. Mater. Res. **45**, 1 (2015).

[5] F. Schwierz, J. Pezoldt, and R. Granzner, Nanoscale **7**, 8261 (2015).

[6] D. Akinwande, C. Huyghebaert, C.-H. Wang, M. I. Serna, S. Goossens, L.-J. Li, H.-S. P. Wong, and F. H. L. Koppens, Nature (London) **573**, 507 (2019).

[7] X. M. Zhang, J. P. Hu, Y. C. Cheng, H. Y. Yang, Y. G. Yao, and S. Y. A. Yang, Nanoscale **8**, 15340 (2016).

[8] N. R. Glavin, R. Rao, V. Varshney, E. Bianco, A. Apte, A. Roy, E. Ringeand, and P. M. Ajayan, Adv. Mater. **32**, 2070052 (2020).

[9] B. Huang, G. Clark, E. Navarro-Moratalla, D. R. Klein, R. Cheng, K. L. Seyler, D. Zhong, E. Schmidgall, M. A. McGuire, D. H. Cobden, W. Yao, D. Xiao, P. Jarillo-Herrero, and X. Xu, Nature (London) **546**, 270 (2017).

[10] C. Gong, L. Li, Z. Li, H. Ji, A. Stern, Y. Xia, T. Cao, W. Bao, C. Wang, Y. Wang, Z. Q. Qiu, R. J. Cava, S. G. Louie, J. Xia, and X. Zhang, Nature (London) **546**, 265 (2017).

[11] K. L. Seyler, D. Zhong, D. R. Klein, S. Gao, X. Zhang, B. Huang, E. Navarro-Moratalla, L. Yang, D. H. Cobden, M. A. McGuire, W. Yao, D. Xiao, P. Jarillo-Herrero, and X. Xu, Nat. Phys. **14**, 277 (2018).

[12] C. Cardoso, D. Soriano, N. A. Garcí-Martínez, and J. Fernández-Rossier, Phys. Rev. Lett. **121**, 067701 (2018).

[13] X. Li, P. Li, V. D. H. Hou, M. DC, C.-H. Nien, F. Xue, D. Yi, C. Bi, C.-M. Lee, S.-J. Lin, W. Tsai, Y. Suzuki, and S. X. Wang, Matter **4**, 1639 (2021).

[14] S. Bertolazzi, P. Bondavalli, S. Roche, T. San, S.-Y. Choi, L. Colombo, F. Bonaccorso, and P. Samor, Adv. Mater. **31**, 1806663 (2019).

[15] G. Hu and B. Xiang, Nanoscale Res. Lett. **15**, 226 (2020).

[16] C.-C. Chiang, V. Ostwal, P. Wu, C.-S. Pang, F. Zhang, Z. Chen, and J. Appenzeller, Appl. Phys. Rev. **8**, 021306 (2021).

[17] P. Huang, P. Zhang, S. Xu, H. Wang, X. Zhang, and H. Zhang, Nanoscale **12**, 2309 (2020).

[18] J. Seo, D. Y. Kim, E. S. An, K. Kim, G.-Y. Kim, S.-Y. Hwang, D. W. Kim, B. G. Jang, H. Kim, G. Eom *et al.*, Sci. Adv. **6**, eaay8912 (2020).

[19] J. Liu, Z. Liu, T. Song, and X. Cui, J. Mater. Chem. C **5**, 727 (2017).

[20] M. Ashton, D. Gluhovic, S. B. Sinnott, J. Guo, D. A. Stewart, and R. G. Hennig, Nano Lett. **17**, 5251 (2017).

[21] X. T. Wang, Z. X. Cheng, G. Zhang, H. K. Yuan, H. Chen, and X.-L. Wang, Phys. Rep. **888**, 1 (2020).

[22] Y. Feng, X. Wu, J. Hana, and G. Gao, J. Mater. Chem. C **6**, 4087 (2018).

[23] Z. Chen, X. Fan, Z. Shen, Z. Luo, D. Yang, and S. Ma, J. Mater. Sci. **55**, 7680 (2020).

[24] J. Yang, S. Zhang, L. Li, A. Wang, Z. Zhong, and L. Chen, Matter **1**, 1 (2019).

[25] G. Rahman and Z. Jahangirli, Phys. Status Solidi RRL **14**, 1900509 (2020).

[26] X.-Y. Li, M.-H. Zhang, M.-J. Ren, and C.-W. Zhang, Phys. Chem. Chem. Phys. **22**, 27024 (2020).

[27] P. Li, Phys. Chem. Chem. Phys. **21**, 6712 (2019).

[28] A. Hashmi, K. Nakanishi, M. U. Farooq, and T. Ono, npj 2D Mater. Appl. **4**, 39 (2020).

[29] S.-S. Wang, Z.-M. Yu, Y. Liu, Y. L. Jiao, S. Guan, X.-L. Sheng, and S. Y. A. Yang, Phys. Rev. Mater. **3**, 084201 (2019).

[30] W.-X. Ji, B.-M. Zhang, S.-F. Zhang, C.-W. Zhang, M. Ding, P.-J. Wang, and R. Q. Zhang, Nanoscale **10**, 13645 (2018).

[31] T. He, X. Zhang, Y. Liu, X. Dai, and G. Liu, Phys. Rev. B **102**, 075133 (2020).

[32] M. Z. Hasan and C. L. Kane, Rev. Mod. Phys. **82**, 3045 (2010).

[33] X. L. Qi and S. C. Zhang, Rev. Mod. Phys. **83**, 1057 (2011).

[34] A. A. Burkov and L. Balents, Phys. Rev. Lett. **107**, 127205 (2011).

[35] X. Wan, A. M. Turner, A. Vishwanath, and S. Y. Savrasov, Phys. Rev. B **83**, 205101 (2011).

[36] Z-M. Yu, Y. Yao, and S.A. Yang, Phys. Rev. Lett. **117**, 077202 (2016).

[37] L. Jin, X. M. Zhang, Y. Liu, X. F. Dai, L. Y. Wang, and G. D. Liu, Phys. Rev. B **102**, 195104 (2020).

[38] Y. Chen, X. Gu, Y. Li, X. Du, L. Yang, and Y. Chen, Matter **3**, 1114 (2020).

[39] J. Y. Liu, S. Wang, and Q. Sun, Proc. Natl. Acad. Sci. USA **114**, 651 (2017).

[40] J. X. Li, H. Ma, Q. Xie, S. B. Feng, S. Ullah, R. Li, J. Dong, D. Li, Y. Li, and X.-Q. Chen, Sci. China Mater. **61**, 23 (2018).

[41] W. Z. Meng, X. M. Zhang, Y. Liu, X. F. Dai, and G. D. Liu, Phys. Rev. B **104**, 195145 (2021).

[42] C. R. Rajamathi, U. Gupta, N. Kumar, H. Yang, Y. Sun, V. Süβ, C. Shekhar, M. Schmidt, H. Blumtritt, P. Werner, B. Yan, S. Parkin, C. Felser, and C. N. R. Rao, Adv. Mater. **29**, 1606202 (2017).

[43] Q. Yang, G. Li, K. Manna, F. Fan, C. Felser, and Y. Sun, Adv. Mater. **32**, 1908518 (2020).

[44] L. R. Wang, X. M. Zhang, W. Z. Meng, Y. Liu, X. F. Dai, and G. D. Liu, J. Mater. Chem. A **9**, 22453 (2021).

[45] W. Liu, X. M. Zhang, W. Z. Meng, Y. Liu, X. F. Dai, and G. D. Liu, iScience **25**, 103543 (2021).

[46] H. Weng, Y. Liang, Q. Xu, R. Yu, Z. Fang, X. Dai, and Y. Kawazoe, Phys. Rev. B **92**, 045108 (2015).

[47] S. A. Yang, H. Pan, and F. Zhang, Phys. Rev. Lett. **113**, 046401 (2014).

[48] C. Fang, H. M. Weng, X. Dai, and Z. Fang, Chin. Phys. B **25**, 117106 (2016).

[49] Y. Kim, B. J. Wieder, C. L. Kane, and A. M. Rappe, Phys. Rev. Lett. **115**, 036806 (2015).

[50] X. M. Zhang, Z.-M. Yu, X.-L. Sheng, H. Y. Yang, and S. Y. A. Yang, Phys. Rev. B **95**, 235116 (2017).

[51] L. Jin, X. M. Zhang, Y. Liu, X. F. Dai, X. N. Shen, L. Y. Wang, and G. D. Liu, Phys. Rev. B **102**, 125118 (2020).

[52] H. P. Zhang, X. M. Zhang, Y. Liu, X. F. Dai, G. Chen, and G. D. Liu, Phys. Rev. B **102**, 195124 (2020).

[53] T. L. He, X. M. Zhang, T. Yang, Y. Liu, X. F. Dai, and G. D. Liu, Phys. Rev. Mater. **5**, 024205 (2021).

[54] Z.-M. Yu, Z. Zhang, G.-B. Liu, W. Wu, X.-P. Li, R.-W. Zhang, S. Y. A. Yang, and Y. G. Yao, Sci. Bull. **67**, 375 (2022).

[55] S. Li, Z.-M. Yu, Y. Liu, S. Guan, S.-S. Wang, X. Zhang, Y. Yao, and S. A. Yang, Phys. Rev. B **96**, 081106(R) (2017).

[56] L. R. Wang, L. Jin, G. D. Liu, Y. Liu, X. F. Dai, and X. M. Zhang, Appl. Mater. Today **23**, 101057 (2021).

[57] X. M. Zhang, Z. M. Yu, Y. H. Lu, X. L. Sheng, H. Y. Yang, and S. A. Yang, Phys. Rev. B **97**, 125143 (2018).

[58] J. Shang, Y. Liang, L. Yang, J. Li, and D. Liang, Solid State Commun. **310**, 113839 (2020).

[59] S. Jeon, Y.-T. Oh, and Y. Kim, Phys. Rev. B **100**, 035406 (2019).

[60] Y.-J. Song and K.-W. Lee, Phys. Rev. B **102**, 035155 (2020).

[61] T. L. He, X. M. Zhang, L. R. Wang, Y. Liu, X. F. Dai, L. Y. Wang, and G. D. Liu, Mater. Today Phys. **17**, 100360 (2021).

[62] X. M. Zhang, L. Jin, X. F. Dai, G. F. Chen, and G. D. Liu, J. Phys. Chem. Lett. **9**, 5358 (2018).

[63] B. B. Zheng, B. W. Xia, R. Wang, J. Z. Zhao, Z. J. Chen, Y. J. Zhao, and H. Xu, npj. Comput. Mater. **5**, 74 (2019).

[64] L. Jin, X. M. Zhang, T. L. He, W. Z. Meng, X. F. Dai, and G. D. Liu, J. Phys. Chem. C **124**, 12311 (2020).

[65] L. Xu, X. M. Zhang, W. Z. Meng, T. L. He, Y. Liu, X. F. Dai, Y. Zhang, and G. D. Liu, J. Mater. Chem. C **8**, 14109 (2020).

[66] G. Kresse and D. Joubert, Phys. Rev. B: Condens. Matter Mater. Phys. **59**, 1758 (1999).

[67] P. E. Blochl, Phys. Rev. B **50**, 17953 (1994).

[68] J. P. Perdew, K. Burke, and M. Ernzerhof, Phys. Rev. Lett. **77**, 3865 (1996).

[69] S. Grimme, and J. Comput. Chem. **27**, 1787 (2006).

[70] A. Togo, F. Oba, and I. Tanaka, Phys. Rev. B: Condens. Matter Mater. Phys. **78**, 134106 (2008).

[71] N. Marzari and D. Vanderbilt, Phys. Rev. B **56**, 12847 (1997).

[72] Q. S. Wu, S. N. Zhang, H.-F. Song, M. Troyer, and A. A. Soluyanov, Comput. Phys. Commun. **224**, 405 (2018).

[73] N. Mounet, M. Gibertini, P. Schwaller, D. Campi, A. Merkys, A. Marrazzo, T. Sohier, I. E. Castelli, A. Cepellotti, G. Pizzi, and N. Marzari, Nat. Nanotechnol. **13**, 246 (2018).

[74] W. Wang, S. Dai, X. Li, J. Yang, D. J. Srolovitz, and Q. Zheng, Nat. Commun. **6**, 7853 (2015).

[75] Z. Fang, X. Li, W. Shi, Z. Li, Y. Guo, Q. Chen, L. Peng, and X. Wei, J. Phys. Chem. C **124**, 23419 (2020).

[76] M. Kar, R. Sarkar, S. Pal, and P. Sarkar, Phys. Rev. B **101**, 195305 (2020).

[77] Y. Jing, Y. Ma, Y. Li, and T. Heine, NanoLett. **17**, 1833 (2017).

[78] N. Miao, B. Xu, N. C. Bristowe, J. Zhou, and Z. Sun, J. Am. Chem. Soc. **139**, 11125 (2017).

[79] S. Zhao, Z. Li, and J. Yang, J. Am. Chem. Soc. **136**, 13313 (2014).

[80] L. Jin, L. R. Wang, X. M. Zhang, Y. Liu, X. F. Dai, H. L. Gao, and G. D. Liu, Nanoscale **13**, 5901 (2021).

[81] X. Zhou, R.-W. Zhang, Z. Zhang, D.-S. Ma, W. Feng, Y. Mokrousov, and Y. G. Yao, J. Phys. Chem. Lett. **10**, 3101 (2019).

[82] W.-B. Zhang, Q. Qu, P. Zhu, and C.-H. Lam, J. Mater. Chem. C **3**, 12457 (2015).

[83] H. L. Zhuang, P. R. C. Kent, and R. G. Hennig, Phys. Rev. B: Condens. Matter Mater. Phys. **93**, 134407 (2016).

[84] L. Liu, C. Wang, J. Li, X.-Q. Chen, Y. Jia, and J.-H. Cho, Phys. Rev. B **101**, 165403 (2020).

[85] R. F. Evans, W. J. Fan, P. Chureemart, T. A. Ostler, M. O. Ellis, and R. W. Chantrell, J. Phys. Condens. Matter. **26**, 103202 (2014).